Effects of rare-earth oxides on grain boundary strength of silicon nitride ceramics

Komaki Matsuura [a], Tatsuki Ohji [a,b,*], Takuma Takahashi [a,c], Motoyuki Iijima [a], Junichi Tatami [a]

[a] *Yokohama National University, 79-7 Tokiwadai, Hodogayaku, Yokohama, Kanagawa 240-8501, Japan*
[b] *National Institute of Advanced Industrial Science and Technology (AIST), Sakurazaka 4-205, Moriyama-ku, Nagoya, Aichi 463-8560, Japan*
[c] *Kanagawa Institute of Industrial Science and Technology, 705-1 Shimoimaizumi, Ebina, Kanagawa 243-0435, Japan*

ARTICLE INFO

ABSTRACT

This study investigates the grain boundary (GB) strengths for Si_3N_4 ceramics doped with 3 wt% RE_2O_3 (RE = Y, La, or Lu) and 7 wt% MgO, using microcantilever beam specimens having different misorientation angles of the two adjacent grains. The measured strengths are so high that they are comparable to the theoretical strength of the intergranular glassy film (IGF). They are also widely scattered with a Weibull modulus of 3.0. The strength depends on the type of RE_2O_3 and increases in order of Y<La<Lu. It is suggested that the fracture occurs from the IGF/Si_3N_4 interfaces rather than within the IGF, and that O anions, which reside within the IGF and do not dissolve into the β-Si_3N_4 crystal lattice because of the high cationic field strength, reduce the IGF/grain interface strength. The GB strength also little depends on the misorientation angles, which is discussed in relation with the IGF accommodation ability of mismatch.

1. Introduction

Silicon nitride (Si_3N_4) ceramics have been employed for a wide variety of engineering applications including wear-resistant parts, high-temperature components, metal-cutting tools, orthopedic implants, heat-dissipating substrates, and electronics manufacturing tools [1–13], owing to their excellent mechanical reliability, high thermal conductivity, good heat and corrosion resistances, high electric insulation, low density, etc. Si_3N_4 ceramics are typical difficult-to-sinter materials and therefore they are usually produced by using sintering additives such as oxide ceramics. The additives form liquid phase at elevated temperatures, which enhances the solution-reprecipitation processes leading to the densification during sintering. Upon cooling, the liquid remains as intergranular glassy film (IGF) between two grains and secondary crystal or amorphous phases at multi-grain junctions. The IGF thickness ranges in 0.5 nm to 1.5 nm, depending on the film chemistry [14–18]. These grain boundaries (GBs) play a critical role in determining mechanical properties of Si_3N_4 ceramics.

In the recent years, many of the Si_3N_4 parts used in advanced applications are becoming smaller and thinner. For example, Si_3N_4

ceramics have been applied to heat-dissipating substrates of power devices [10], and their thickness is now reduced to 200 μm or less for enhancing the heat dissipation. Si_3N_4 thin films are being used for permeation barrier, encapsulation and passivation in a wide range of advanced applications including microelectronics manufacturing, silicon solar cells, and microelectrode arrays [11–13]. For such microscale applications, the mechanical behavior of the GBs becomes more influential in governing the structural reliabilities, and therefore, it is essential to precisely evaluate and understand them.

The microcantilever bending test is a powerful technique that can measure mechanical properties of ceramic materials at microscale [19–30]. A load is applied at the tip of a microcantilever beam specimen to generate the bending stress on the top surface of the specimen. This method has been employed to investigate microscale mechanical performance of Si_3N_4 ceramics [20,22,26,27,29]. Tatami et al. [20] investigated fracture toughness of Si_3N_4 ceramics doped with RE_2O_3 (RE: Lu, Y, or La) and Al_2O_3 using single-edge notched microcantilever beam specimens and revealed that the GB toughness value increased with increasing the ionic radius (Lu<Y<La). Csanádi et al. [26] studied microscale fracture strength of grains and GBs in La-doped Si_3N_4

---

ceramics; the GB strength with increasing the La_2O_3 content, confirming that the existence of RE cations weakens the GBs. Tanabe et al. [27] evaluated the deformation behaviors and fracture strength of β-Si_3N_4 single crystals having different angles of tensile-stress application from the *c*-axis and elucidated their dependence on the crystal orientations. This technique is also effective for evaluating microscopically the time-dependent degradation behaviors of Si_3N_4 ceramics such as corrosion in combination with the mechanical properties, enabling their rapid assessment [22,29].

Al_2O_3, which was used in the above-stated study of Tatami et al. [20], is one of the most frequently employed sintering additives for producing Si_3N_4 ceramics. It has been known that, when this oxide is doped as a sintering additive, β-SiAlON layer forms on β-Si_3N_4 grains and has a potential to be strongly chemically bonded to GB phases, significantly affecting GB mechanical behavior. When, however, giving a high thermal conductivity (TC) to Si_3N_4 ceramics for the above-mentioned heat-dissipating substrates of power devices, MgO in place of Al_2O_3 was used since Al is dissolved into Si_3N_4 crystals, making oxygen vacancies and reducing the TCs.

This study addresses fracture strength of GBs for Si_3N_4 ceramics doped with RE_2O_3 (RE = La, Y, or Lu) and MgO using microcantilever beam specimens. For the above reason, the combination of rare earth oxides and MgO is most frequently employed as sintering additives for high-TC Si_3N_4 ceramics. Because of the absence of the β-SiAlON layer formation, this sintering additive system is able to give us the pure information on the effects of the rare-earth oxides on the GB strength.

2. Experimental

2.1. Preparation and characterization of Si_3N_4 ceramics

Si_3N_4 ceramics were prepared by adding RE_2O_3 (RE=La, Y, or Lu; RU-P; Shin-Etsu Chemical Co., Ltd., Tokyo, Japan) and MgO (500 A, Ube Co. Ltd., Tokyo, Japan) powders to α-Si_3N_4 powder (SN-E10, Ube Co. Ltd., Tokyo, Japan) in a weight ratio of 3:7:90. These powders were mixed with a dispersant (2 wt%; polyacrylic acid; Celuna E503, Chukyo Yushi Co., Ltd., Japan) and ball-milled in ethanol for 48 h. Dioctyl phthalate (2 wt%; Wako Pure Chemicals Co., Japan) and paraffin (4 wt %; melting point: 46 °C-48 °C; Junsei Chemical Co., Ltd., Japan) were added as the lubricant and binder, respectively. Granules of the powder mixtures were prepared by forced sieving through a nylon mesh with a 250 μm mesh opening. Subsequently, they were molded by uniaxial pressing at 50 MPa for 30 s, followed by cold isostatic pressing at 200 MPa for 1 min to produce disk-shaped green bodies of ϕ15 mm × 3 mm thickness. The green bodies were dewaxed at 250 °C for 3 h and at 500 °C for 3 h in air and subsequently sintered at 1950 °C for 6 h in 0.9 MPa N_2, using a multi-purpose sintering furnace (Hi-Multi 5000, Fujidempa Kogyo Co., Ltd., Osaka, Japan). The sintered samples doped with Y_2O_3, La_2O_3 and Lu_2O_3 (plus MgO) are denoted by SN-Y, SN-La, and SN-Lu, respectively, hereafter.

The bulk density was measured according to the Archimedes principle with water displacement. Relative densities were calculated through dividing the measured bulk densities by a theoretical density. The constituent crystal phases of the fabricated Si_3N_4 ceramics were identified by X-ray diffraction (XRD) patterns using an X-ray diffractometer (Multiflex, Rigaku Corporation, Tokyo, Japan) with Cu Kα (λ = 1.5406 Å) radiation, on a plane perpendicular to the polished surface. A scanning electron microscopy (SEM; JSM-6390LV, JEOL Ltd., Japan) was performed to observe the microstructures of the specimens polished and plasma etched by CF_4 gas.

TC was determined by a laser flash method according to ISO 18755:2022, using a thermal constant measurement system (TC-9000H, ULVAC, Inc., Chigasaki, Japan) through measuring thermal diffusivity and specific heat. Square plate specimens of approximately 7 mm × 7 mm × 1 mm were cut from the sintered bodies and were sputter-coated with a 100 nm thick Au film to prevent direct transmission of the laser

(Ion Sputter E-1030, Hitachi, Ltd., Tokyo, Japan), followed by a carbon coating to increase the amount of energy absorbed. TC, κ, was calculated according to the equation, $\kappa = \rho C_p \alpha$, where ρ is the bulk density of the specimen obtained by the Archimedes method, C_p is the specific heat, and α is the thermal diffusivity obtained by the laser flash method.

2.2. Determination of mechanical properties

The aim of this study is to investigate the GB strength of the Si_3N_4 ceramics, and thus it is essential to identify an appropriate GB to be observed. For this purpose, the crystallographic orientation of the β-Si_3N_4 crystal grains on the sample surfaces was identified by electron beam backscatter diffraction (EBSD) using a field emission scanning electron microscope (FE-SEM; JSM-7001F, JEOL Ltd., Japan). The obtained Kikuchi patterns were analyzed using software (OIM Data Collection and OIM Data Analysis, AMETEK, USA). The samples were ground and mirror-polished to a thickness of approximately 0.5 mm, and then polished by ion milling (Cross Section Polisher, SM-09010, JEOL Ltd., Japan). The processed samples were coated with a carbon coater (Carbon Coater, CADE-E, Meiwafosis Co., Ltd., Japan). An example of the obtained inverse pole figure (IPF) map of the grains is shown in Fig. 1(a). GBs where the *c*-axes of two grains intersect each other are selected as the target GBs, and microcantilever beam specimens are machined using an FIB-SEM (Crossbeam 550, Carl Zeiss AG, Germany) so that their fixed-ends where the maximum tensile stress arises are at the target GBs with the *c*-axis of the support-side grain being perpendicular to the specimen's longitudinal direction. This results in specimens having different angles, θ_{axis}, between the two intersecting-*c*-axes, as show in Fig. 1(b). This study employed two types of specimens, (*R*) and (*S*), with different sizes as shown in Table 1; The specimens (*S*), whose volume is ~1/6 of (*R*), were prepared only for SN-Y. Fig. 2(a) and
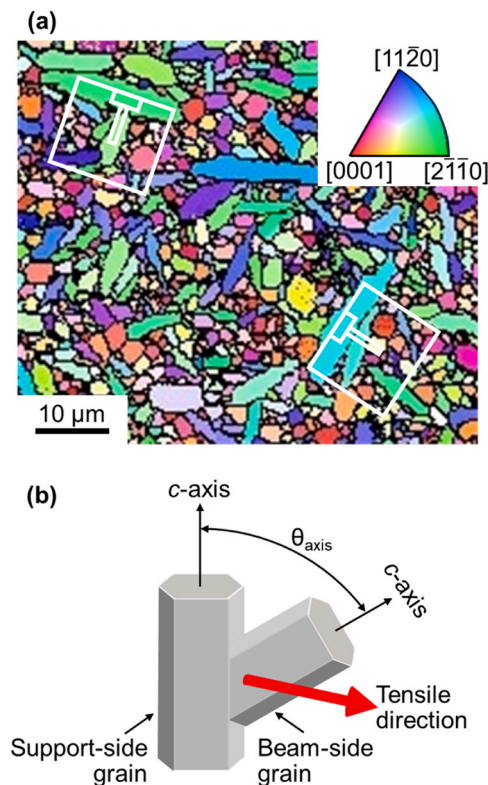

Fig. 1. (a) Inverse pole figure map of β-Si_3N_4 grains and two examples of specimen extractions. (b) Schematic illustration of support-side and beam-side grains with an angle between the two intersecting-*c*-axes, θ_{axis}, and tensile direction.

Table 1

Sizes of microcantilever beam specimens (R) and (S).

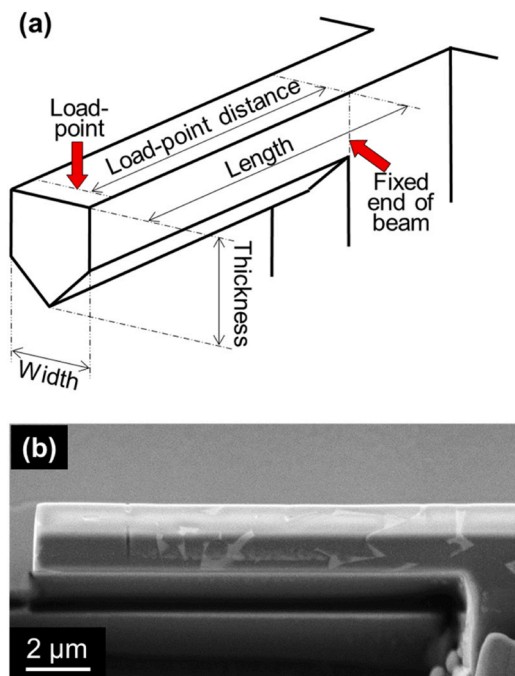| Specimen	SN-Y (R)	SN-Y (S)	SN-La (R)	SN-Lu (R)
Width, μm	1.45 ± 0.25	0.82 ± 0.16	1.53 ± 0.23	1.69 ± 0.08
Thickness, μm	2.01 ± 0.28	1.14 ± 0.08	2.11 ± 0.18	2.10 ± 0.16
Length, μm	14.15 ± 0.81	6.64 ± 0.64	13.00 ± 0.53	14.58 ± 0.69
Load-point distance, μm	10.25 ± 0.55	5.17 ± 0.18	10.17 ± 0.60	10.22 ± 0.17

Fig. 2. (a) Schematic illustration of a microcantilever beam specimen. (b) Example of the specimen (R). The width, thickness, and length were approximately 1.5, 2.5, and 12 μm, respectively.

(b) show a schematic illustration of the specimens and an example of (R), respectively. The section profile was pentagonal.

The bending tests were carried out using a nano-indenter (TI-Premier Triboindenter, Bruker, USA), and the load was applied using a cube corner-type diamond indenter with a displacement rate of 30 nm/s at the load point distances from the fixed end of beam (Table 1). The relationship between the load and displacement was obtained through a bending test conducted on the specimens. The measured displacements of the indenter generated during the bending test include both the depth of the indent itself and the deflection of the specimen at the loading point. Therefore, the true displacement at the loading point was obtained by subtracting the indentation depth measured when the indentation was made on a flat surface of the same specimen using the same diamond indenter with the same load, following the procedure described in the previous work [27].

The bending stress, σ, and the strain, ε, of the specimen are calculated using the following equations based on the elastic beam theory:

$$\sigma = \frac{PL\delta}{I} \tag{1}$$

$$\varepsilon = \frac{3d\delta}{L^2} \tag{2}$$

where P is the applied load, L is the load-point distance, δ is the distance between the top surface and the neutral plane, I is the second moment of area calculated for the cross section, and d is the displacement at the loading point. The sectional shape and sizes of each specimen were determined precisely for rigorous calculation of I, using a trapezoidal approximation [30]. The bending strength (or fracture strength) was determined from the maximum load using Eq. (1). The fracture surfaces after the tests were observed by FE-SEM (SU8010, Hitachi High-Tech Corp., Japan).

3. Results

3.1. Densities, crystalline phases, microstructures, and TCs

The measured relative densities of the obtained three samples of SN-Y, SN-La and SN-Lu are shown in Table 2. All the densities are sufficiently high, indicating the nearly fully densified bodies. Fig. 3 shows the XRD profiles for constituent crystalline phases of SN-Y, SN-La, and SN-Lu. The phase identification showed that the major phase in all the samples is β-Si$_3$N$_4$ with melilite phase (Y$_2$Si$_3$O$_3$N$_4$) in SN-Y and J phase (Lu$_4$Si$_2$O$_7$N$_2$) in SN-Lu, as GB crystalline phases.

Fig. 4 shows SEM photographs of microstructures of SN-Y, SN-La, and SN-Lu. Dense microstructures of large, elongated β-Si$_3$N$_4$ grains (>10 μm) embedded in equiaxed matrix ones are obtained in all the samples. It should be noted that, because of grain growth during sintering for 6 h at 1950 °C, the grain size is relatively large. There are, however, some differences in terms of the grain morphologies among the samples; the large grains of SN-Lu tend to have lower aspect ratios than SN-Y and SN-La. In addition, the grains with higher aspect ratios

Table 2

Measured relative densities, thermal conductivities, and bending strength of SN-Y, SN-La, and SN-Lu. "n" is the number of specimens, and the value after " ± " is the standard deviation. Differential binding energies (Si reference), DBE, and cationic field strengths, CFS, of RE ions of sintering additives are also shown.

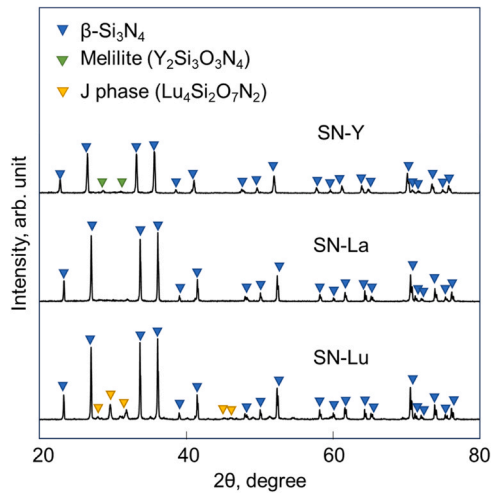|	SN-Y		SN-La	SN-Lu
Relative density, %	98.4		97.9	98.6
TC, W/(mK)	89.0		79.5	81.2
	SN-Y (R)	**SN-Y (S)**	**SN-La (R)**	**SN-Lu (R)**
Bending strength, GPa	7.8 ± 2.1	14.2 ± 2.6	9.3 ± 2.0	11.7 ± 1.9
	(n = 6)		(n = 4)	(n = 6)
		(n = 6)		
Target GB	9.0 ± 1.3	ditto	10.4 ± 0.9	12.1 ± 1.7
	(n = 4)		(n = 3)	(n = 5)
Off-target GB	5.3 ± 0.3	-	6.1	9.3
	(n = 2)		(n = 1)	(n = 1)
DBE of RE, eV	~0		-0.98	2.50
CFS of RE, Å^{-2}	2.77		2.18	3.19

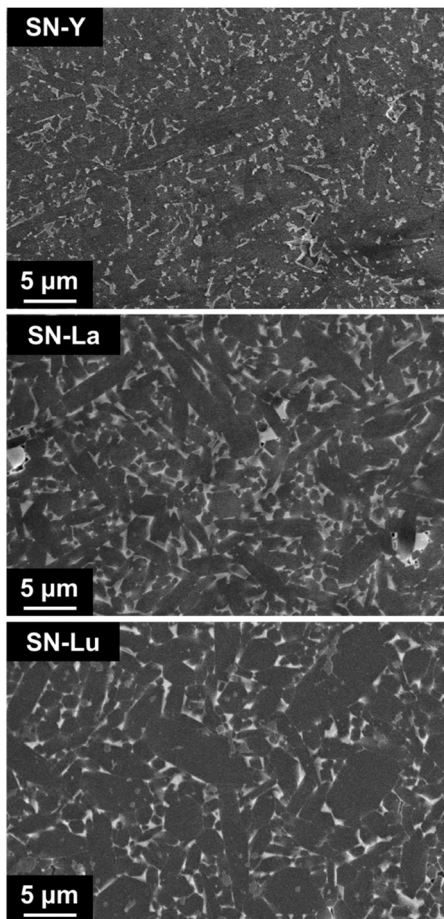**Fig. 3.** XRD profiles of SN-Y, SN-La, and SN-Lu.

Fig. 4. SEM photographs of microstructures of SN-Y, SN-La, and SN-Lu.

are seen more frequently in SN-La, though the difference between SN-La and SN-Y is small.

The measured TCs of the samples are shown also in Table 2. They range from ~80 W/(m·K) to ~90 W/(m·K), which agrees with the values reported so far as TC of Si_3N_4 ceramics sintered from α-powder with RE oxides and MgO under the above-described conditions [31,32]. The value of SN-Y is ~10 W/(m·K) higher than those of SN-La and SN-Lu, which can be considered as a significant difference in TCs of Si_3N_4 ceramics.
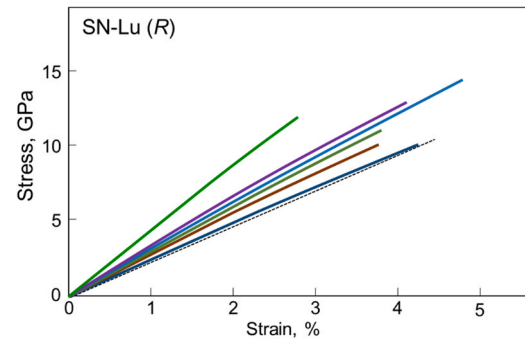

Fig. 5. Stress-strain diagrams of microcantilever bending tests for SN-Lu (R). A dashed straight line is attached to the bottom one.

3.2. Bending strength

All the stress-strain diagrams obtained using Eqs. (1) and (2) from the load-displacement relations measured in this study showed that the stress increased with increasing the strain until the fracture occurred, demonstrating brittle fracture nature. Fig. 5 shows the stress-strain diagrams of SN-Lu (R) as examples. However, the diagrams were not completely linear but contained very slight curvatures; The bottom diagram compared with the dashed straight line shows a non-linearity. It is also known, from Fig. 5, that the maximum stresses, or fracture strengths, are widely scattered.

Tanabe et al. [27] revealed that β-Si_3N_4 single crystals can deform in the primary slip system with the CRSS of 1.34 GPa; the yield stress ranged in 2 GPa to 17 GPa, depending on the crystal orientation. For polycrystals to deform uniformly without failure at the GBs, however, five independent slip systems must operate according to the von Mises criterion [33] (it should be noted that a recent review on this subject indicated that three linearly independent slip systems are essentially sufficient for compatible deformation [34]). Because Si_3N_4 polycrystals do not satisfy this criterion (even three independent slip systems), they do not deform in principle. It should be noted, however, that the grain sizes of the samples used in this study are so large that the number of the grains contained in a microcantilever beam specimen is limited. Fig. 6(a) shows a front view of a beam specimen of this study, in comparison of that of Fujita et al. [17] (Fig. 6(b)), whose load-displacement (or stress-strain) diagrams were completely linear. Only a couple of grains are seen in (a), and the large parts of their surfaces are exposed as the specimen surface, allowing such parts to deform to a small extent. It is most likely that this results in the slight curvatures observed in the stress-strain diagrams. On the other hand, in (b), a relatively large number of grains are observed, and they are constrained by the surrounding grains, resulting in the linear relationship [22].
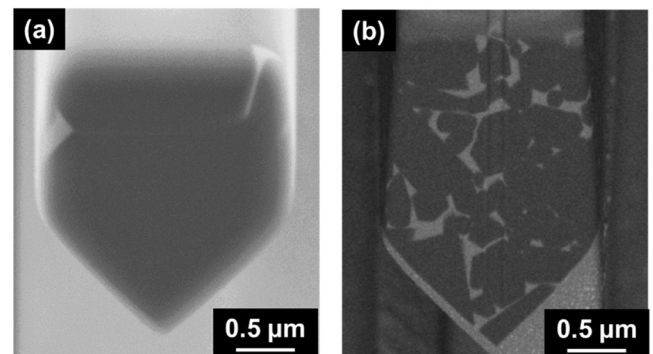

Fig. 6. Front view of a microcantilever beam specimen used in this study (a), in comparison with that in Fujita et al. [22].

The calculated bending strength values are listed in Table 2. The strength increases in order of Y<La<Lu for the specimens (R) with relatively significant differences; SN-Lu (R)'s strength is 50 % higher than SN-Y (R)'s. As will be shown in Section 3.3, fractographic studies revealed that all the fractures occurred from GBs, indicating that the values listed in Table 2 are GB strength. The fracture origins of the specimens (R), however, were divided into the target GBs and the GBs other than the targets (off-target GBs), as shown in Table 2. The strengths with fractures from the target GBs are higher than those from the off-target ones for all the three samples, and the former strength also increases in order of Y<La<Lu. In terms of SN-Y (S), all the fractures occurred from the target GBs. Theoretical studies on IGF of Si_3N_4 ceramics using molecular dynamics [35,36] and ab initio [37] methods showed that the fracture strength ranged from 10 GPa to 25 GPa depending on the composition, film thickness, crystallographic orientation, etc. The measured strengths of the target GBs, particularly those of SN-Y (S), 14.2 ± 2.6 GPa, are so high that they are almost comparable to theoretically determined values.

The bending strength of β-Si_3N_4 single crystals determined using the same microcantilever beam specimens as the specimens (R) ranged in 5 GPa to 22 GPa, depending on the crystal orientation [27], which also are comparable to the GB strength of this study. However, the fracture process of the single crystals is heavily involved with the dislocation pileups, which lower their bending strength. Such dislocation pileups are not produced in the polycrystals because of the constraint by the surrounding grains (though, as above stated, slight dislocation occurs in the microcantilever bending tests of this study). Thus, it can be presumed that the β-Si_3N_4 grains in the polycrystals have higher strength than the above values, 5–22 GPa. This most likely leads to the result that all the fractures occurred from GBs in this study.

Fig. 7 shows the bending strength for SN-Y (R), SN-Y (S), SN-La (R) and SN-Lu (R) as a function of the angle between the two intersecting-c-axes, θ_{axis} (Fig. 1(b)). The dependence on θ_{axis} is little observed and the value is almost constant irrespective of the angle for the specimens (R) of all the three samples. In terms of the specimens (S) as well, the angle dependence is almost negligible, while their plots are high compared to those of (R). The wide dispersion of the bending strength is recognizable in Fig. 7 as well.

3.3. Fracture surface observation

As stated in Section 3.2, fractographic studies were carried out for the fracture origins of all the specimens after the bending tests. The fracture surfaces for the specimens (R) were divided into two categories: fractures successfully occurring from the target GBs and those from the
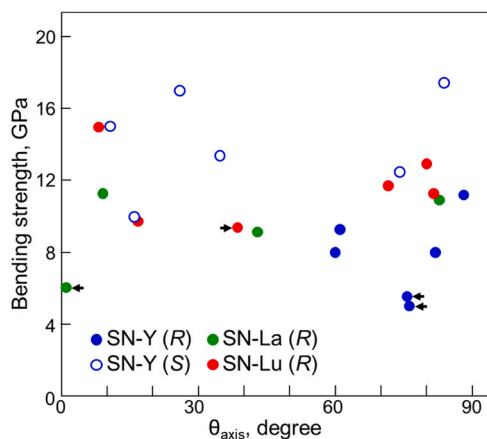

Fig. 7. Bending strength of SN-Y (R), SN-Y (S), SN-La (R), and SN-Lu (R) as a function of the angle between the two intersecting-c-axes, θ_{axis}. The arrow indicates the strength from off-target GBs.
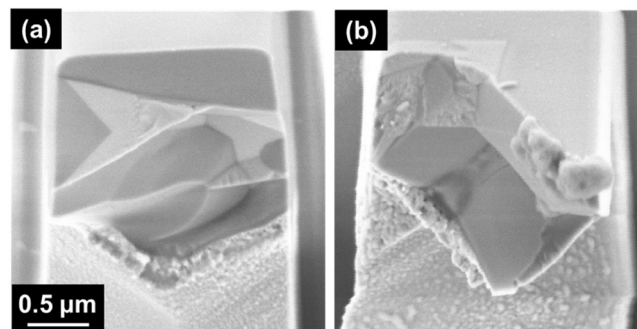

Fig. 8. Examples of fracture surfaces; (a) Flat surface and (b) uneven surface.
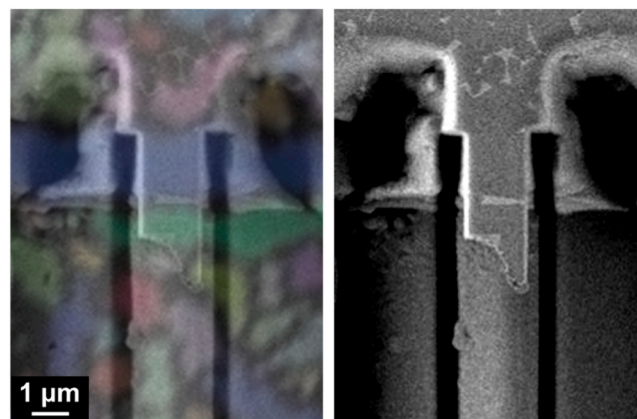

Fig. 9. Example of a top surface of a fractured specimen with its EBSD-IPF map, whose fracture surface is given in Fig. 8(b).

origins out of the target ones. As shown in Table 2, most of the fractures are categorized as the former. Examples of the former and latter are shown in Fig. 8(a) and (b), respectively. The flat surface along the target GB is identified in (a), while the fracture origin is apart from the fixed end of beam in (b). In order to identify the locations of the fracture origins, the SEM image of the top surface of the fractured specimen was compared with the EBSD-IPF map. Fig. 9 shows an example of a top surface of a fractured specimen with its EBSD-IPF map, whose fracture surface is given in Fig. 8(b). It was revealed that all the latter fractures occurred from GBs other than the targets (off-target GBs) nearby to the fixed end of beam, including multi-grain junctions (glass phase, secondary crystal phase such as $Y_2Si_3O_3N_4$ and $Lu_4Si_2O_7N_2$, etc.), and that none were from grain insides. As for the specimens (S), all the fractures occurred from the target GBs, as already noted.

4. Discussion

4.1. Effects of RE oxides on microstructures

The influence of different rare earths on grain aspect ratios of Si_3N_4 ceramics has been experimentally characterized by many researchers [38–49]. Painter et al. [40] introduced a first-principles-based energy parameter, differential binding energy (DBE), and it has been known that the grain aspect ratios measured for various rare earth additions in Si_3N_4 ceramics correlate well with the corresponding DBE values. When the DBE value of an RE cation is negative, it is more energetically favorable for the cation to segregate to the nitrogen-rich grain surfaces than Si. On the other hand, a cation with a positive DBE has a greater affinity for O than Si and tends to reside within the IGF. Some studies using atomic-resolution STEM (scanning transmission electron

microscope) on the segregation behavior and specific adsorption sites for RE cations confirmed this theory [41–45]. The RE cations segregating to the grain surfaces hinders the grain growth in the *a*-axis direction, resulting in a higher aspect ratio. The DBE values (Si reference) for La, Y and Lu are shown in Table 2, indicating that the aspect ratio becomes higher in order of Lu<Y<La. This agrees with the above microstructure observations of SN-Y, SN-La, and SN-Lu.

4.2. Effects of RE oxides on TCs

The measured TCs of the samples are shown also in Table 2; SN-Y shows a high value than the others. TCs of Si_3N_4 ceramics are affected by many structural factors including grain sizes and shapes, lattice defects (impurity atoms, vacancies, dislocations, stacking faults, etc.) and GB phases (glassy phases, secondary crystal phases, etc.) [50]. It is known that β-Si_3N_4 grains have a significant anisotropy in TC; for example, Hirosaki et al. [51] estimated the theoretical value to be 170 and 450 W/(m·K) along the *a* and *c* axes, respectively, by using molecular dynamics simulations. In addition, IGF, which exists at GBs of Si_3N_4 ceramics with a typical thickness of 1 nm, has very low TCs around 1 W/(m·K) [52]. Therefore, for obtaining a higher TC in Si_3N_4 ceramics, it is advantageous to have large β-Si_3N_4 grains having high aspect ratios. The microstructural observation revealed that the aspect ratio of large grains tended to increase in order of Lu<Y<La (Y and La are nearly equal), which agrees with the DBE theory as already discussed. Then, SN-Lu is the least advantageous for a high TC in terms of the microstructure. SN-Y contains melilite phase as GB crystalline phase, whose TC is ~10 W/(mK), somewhat higher than that of glass, but SN-Lu does J phase of a similar TC.

Another important factor that affects TC of Si_3N_4 ceramics is the lattice oxygen content, and the TC decreases when this content increases. It is known that the lattice oxygen content decreases with an increase in the cationic field strength (CFS), σ_{CFS} [53], which is given by:

$$\sigma_{CFS} = \frac{Z}{r_i{}^2} \tag{3}$$

where *Z* is the valence of the RE cation and r_i its ionic radius. As the CFS increases, the RE cations attract more oxygen anions in GB glassy phases (both IGF and glass at multi-grain junctions), preventing the dissolution of oxygen atoms into the β-Si_3N_4 crystal lattice. Table 2 shows the calculated CFS, for La, Y, and Lu [54,55]. The CFS increases in order of La<Y<Lu, indicating that Si_3N_4 ceramics containing these elements tend to have a higher TC in this order. Since SN-Y has an RE-CFS higher than, and a microstructure almost equivalent to, those of SN-La, the former shows a higher TC than the latter. SN-Lu is superior to the other two for the RE-CFS but inferior for the microstructural factor as above-stated, resulting in the intermediate TC due to the counter-balance effect.

4.3. Effects of RE oxides on GB strengths

As listed in Table 2, the GB strength is divided into two categories in the specimens (*R*): the fractures from the target GBs (solely comprising intergranular fractures) and those from the off-target ones (including fractures from multi-grain junctions). All are categorized as the former in (*S*). In this discussion, we focus on the former strength as the intergranular strength. The results showed it increased in order of Y<La<Lu. This order agrees with the study by Satet et al. [46], who investigated influence of intergranular phase composition on fracture toughness of Si_3N_4 ceramics using MgO and RE_2O_3 (RE=La, Y, Lu, etc.) as sintering additives. In their study, the microstructure was tailored to have the same grain sizes and morphologies by adjusting the sintering parameters, so that the fracture toughness reflects the debonding behavior of the GB. The toughness increased in order of Lu<La<Y, from which they predicted that the intergranular strength decreased in Lu>La>Y.

If a fracture occurs from an intergranular boundary, it originates either within the IGF or at the IGF/grain interface. As for the former case, we consider the effects of RE cations on the strength of IGF. It is known that the mechanical properties of oxynitride glasses containing RE cations in general appear to vary linearly with the above described CFS (Table 2). The CFS increases in order of La<Y<Lu, and then the strength of IGF is considered to increase in this order. In terms of the IGF/grain interface, it is known that its strength is affected by the RE cations which segregate to the grain surfaces in Si_3N_4 ceramics. As discussed in Section 4.1., this segregation behavior has been well addressed by the DBE theory [40], and since the DBE value (Table 2) increases in order of La<Y<Lu, the amount of the RE cations which segregate to the IGF/grain interface and replace Si ions decreases in this order. Because the RE cations work as glass network modifiers rather than network formers such as Si ions [56,57], their presence weakens the IGF/grain interface. Thus, the DBE theory also predicts that the IGF/grain interface strength increases in order of La<Y<Lu.

Tatami et al. [20] investigated fracture toughness of GBs for Si_3N_4 ceramics doped with 5 wt% RE_2O_3 (RE=La, Y, or Lu) and 3 wt% Al_2O_3 using single-edge notched microcantilever beam specimens and revealed that the measured value increased in order of La<Y<Lu, which agrees with the above order which both the CFS and DBE predict. It should be noted that the fracture toughness should be proportional to the fracture strength because no toughening effect works in this case. In this study, however, the intergranular strength increased in order of Y<La<Lu; the strength of Y is lower than that of La, as opposed to the CFS and DBE predictions.

Becher et al. [39] reported that the crack propagation path observed in intergranular fractures of Si_3N_4 ceramics doped with Y_2O_3 and Al_2O_3 is shifted from solely the crack propagation path along the IGF/grain interface to a mixture of those along the interface and within the IGF, when increasing the Y_2O_3 to Al_2O_3 ratio. It has been known that a distinct epitaxial β-SiAlON layer readily forms on β-Si_3N_4 grains in Si_3N_4 ceramics doped with Al_2O_3, and that the IGF/SiAlON interfaces have a potential to be more strongly chemically bonded than the IGF/Si_3N_4 interfaces [58]. This is because the Al and O are distributed more gradually across the former interface than across the latter, and the SiAlON contains Al–N, Al–O, and Si–O bonds in addition to Si–N bonds, while the intergranular glass does Si–O, Si–N, Al–N, and Al–O, indicating that similar chemical bonds exist in the two phases [58–60]. Because even in such strong IGF/SiAlON interfaces the fracture from the interfaces is predominant, it can be presumed that most of the fractures originate at the IGF/Si_3N_4 interfaces in Si_3N_4 ceramics without Al_2O_3 such as the materials used in this study.

As discussed in "4.2.", the RE cations attract more oxygen anions in the IGF when the CFS value becomes high. This results in a higher oxygen content in the IGF. Yoshiya et al. [61] studied an IGF composed of silicon oxynitride in Si_3N_4 ceramics by molecular dynamics calculations and revealed that more dangling bonds were generated at the IGF/grain interfaces when the N/(N+O) ratio of the IGF decreased due to the larger chemical and structural mismatch between the IGF and the grain. Because the CFS of Y cations is higher than that of La (Table 2), their IGF contains a higher oxygen content, resulting in more dangling bonds at the IGF/grain interfaces. This indicates that SN-Y has a lower IGF/grain interface strength.

Another factor which affects the strength of intergranular boundaries is oxygen anions dissolved at surface and subsurface of Si_3N_4 grains. Walkosz et al. [62] investigated the interfaces between crystalline β-Si_3N_4 grains and amorphous SiO_2 film using STEM imaging techniques and atomically-resolved EELS (electron energy-loss spectroscopy) and revealed that Si, N, and O atoms arrange in SiO_2 in ways resembling the crystalline structure of Si_3N_4 in the vicinity of the interfaces, and that there is a nonuniform interatomic mixing of oxygen and nitrogen at different atomic sites in the interface with O atoms replacing N at the surface and subsurface of the Si_3N_4 grains. The bond dissociation energy of Si-O, 799.6 kJ/mol, is much larger than that of Si-N, 431.7 kJ/mol

[63], though the substitution of O for N decreases the coordination number of the interfacial Si atoms (N bonds to three Si atoms whereas O bonds two Si atoms). Because of the higher CFS, Y cations attract more O anions than La cations in the IGF, resulting in a smaller amount of O anions dissolved at the surface and subsurface of the Si_3N_4 grains. This can lead to weaker IGF/Si_3N_4 interfaces of SN-Y than those of SN-La.

It should be noted that, when Al_2O_3 is doped as a sintering additive, β-SiAlON layer containing O atoms as a crystal constituent forms on β-Si_3N_4 grains and the attraction of RE cations does little work to O anions. This leads to the intergranular strength increase in order of Y<La<Lu, as predicted by the CFS and DBE and observed by Tatami et al. [20].

Theoretical studies using molecular dynamics revealed that the fracture strength of IGF in Si_3N_4 ceramics is significantly affected by, not only the film chemical composition, but also other factors including the film thickness and the adjacent Si_3N_4 grains' crystal surfaces (prism surfaces, etc.) [35,36]. The film thickness, however, is known to depend solely on the film chemistry (namely, RE oxides in this study) [14–18]. The share of the prism surfaces of the grains in total is determined by the aspect ratio, which also depends on RE oxides [40,47]. Thus, RE oxides, which are used as sintering additives, play a critical role in determining the GB strength.

4.4. Dependence of GB strengths on c-axes angles

Assuming two adjacent Si_3N_4 crystals divided by an IGF, they can face each other at various misorientation angles. The crystallographic structure of the IGF is not random but rather exhibits a form of spatially varying orientational order close to both grains [64]. If the misorientation angle is high, or so called "random" GB and the IGF/Si_3N_4 interface is epitaxially bonded, the IGF needs to be thick in order to accommodate this orientational order. Nevertheless, as already stated, it has been known that the IGF thickness of Si_3N_4 ceramics is constant, irrespective of the misorientation, and solely depends on the film chemistry [14–18]. For example, Kleebe et al. [14], employing analytical and high-resolution transmission electron microscopy (AEM, HREM) techniques, showed no angular dependence of the IGF thickness on grain orientation; all the observed GBs revealed a constant film thickness, although the boundaries observed showed distinct differences in misorientation of the adjacent Si_3N_4 grains. They also noted that this result, the independence of the equilibrium thickness, is unexpected and not predicted by theory [14]. This means that, if the misorientation angle is high, the epitaxy of the IGF/Si_3N_4 interface should be sacrificed to accommodate the mismatch, generating many dangling bonds there and lowering the interfacial strength. Therefore, the strength should be dependent on the misorientation angle. The results obtained in this study, however, show that the intergranular strength, or the strength of the target GBs, is little dependent on the two intersecting-c-axes, θ_{axis} for all the three samples (Fig. 7).

The discussion in Section 4.3. suggested that the fracture origins tend to be at the IGF/Si_3N_4 interfaces rather than within the IGF. It is not entirely clear why the strength of the IGF/Si_3N_4 interfaces is little dependent on θ_{axis}. One of the plausible explanations is formation of atomic short-range ordering at the IGF/Si_3N_4 interfaces [62], as stated in Section 4.3. the atomic layers of the amorphous SiO_2 film reconstruct in the vicinity of the β-Si_3N_4/IGF interfaces to adopt the crystalline form of Si_3N_4. It can be considered that these transient layers have some affinity with the IGF, though they resemble the crystalline structure of Si_3N_4, and help accommodate the mismatch of the adjacent two grains.

Another conceivable interpretation is the IGF accommodation ability, which resolves the mismatch with the relatively small thickness. Yoshiya et al. [65] performed molecular dynamics simulations on IGF of an SiO_2 amorphous structure having a 90°-twist GB in Si_3N_4 ceramics. It was found that the presence of the IGF at the GB significantly decreased the number of dangling bonds generated at the interface due to the grain misorientation; however, the excess energy significantly decreased with

increasing the thickness up to 7.0 Å, while further increase in the thickness did not contribute to a release in the geometric strain energy. This indicates that in cases of smaller misorientations than this, the energy reaches the lower equilibrium point at smaller thicknesses. The HREM study on Si_3N_4 ceramics with SiO_2 revealed that the IGF thickness was 1 nm, independent on glass volume fraction [18]. Thus, it is likely to occur that the influence of the grain misorientation is constant at the interfaces irrespective of its degree, which results in the IGF/Si_3N_4 interfacial strength little dependent on θ_{axis}, as observed in Fig. 7.

4.5. Specimen size effects of GB strengths

The strength of SN-Y (*S*) is ~80 % higher than that of SN-Y (*R*). The higher strength of the smaller specimen as well as the brittle failure characteristics seen in the stress-strain diagrams indicates that the GB strength is governed by the size effect of the specimen based on the weakest linkage theory. The stress-strain diagrams of Fig. 5, the plots of Fig. 7, and the standard deviations of Table 2 also show that the measured strength values for each of the samples scatter widely.

According to the Weibull distribution, the relationship between strengths, σ_1 and σ_2, of two specimens having the respective effective volumes, V_1 and V_2, is expressed by:

$$\frac{\sigma_2}{\sigma_1} = \left(\frac{V_1}{V_2}\right)^{\frac{1}{m}} \tag{4}$$

where *m* is the Weibull modulus. Substituting the strength and effective volume of SN-Y (*S*) for σ_1 and V_1, respectively, and those of SN-Y (*R*) for σ_2 and V_2 (Tables 1 and 2), one can obtain *m*=3.0. Csanádi et al. [26] investigated microscale fracture strength of GBs in La-doped β-Si_3N_4 ceramics doped with La_2O_3 and SiO_2 using microcantilever beam specimens much larger than those of this study (pentagonal cross-sections with 11.7–23.2 μm length, 2.1–6.3 μm width and 2.1–5.7 μm thicknesses). The fracture strength along the GBs ranged from 2.1 GPa to 2.9 GPa, depending on the La_2O_3. Assuming the means of these values for σ_1 and V_1 and those of SN-La (*R*) for σ_2 and V_2 leads to *m*=3.3, exhibiting a good agreement with the above Weibull modulus. Thus, the large discrepancy of the GB strength between this study and Csanádi et al. [23] is most plausibly due to the large difference of the effective volumes of the specimens. This also endorses the above presumption that the GB strength is governed by the size effect of the specimen.

Assuming a Griffith crack in an infinite two-dimensional body, the strength, σ_f, is related to the fracture toughness, K_{IC}, and the crack length, *a*, by $\sigma_f = K_{IC}\sqrt{\pi a}$. The GB fracture toughness was determined to be 1.73 MPa m$^{1/2}$ for Si_3N_4 ceramics doped with 5 wt% Y_2O_3 and 3 wt% Al_2O_3, using single-edge notched microcantilever beam specimens [20]. Adopting this K_{IC} value, the crack length, *a*, is estimated to be 7–40 nm and 3–10 nm for SN-Y (*R*) and (*S*) from their bending strengths, respectively. Thus, it can be presumed that such small flaws with widely scattered sizes exist along the GBs and work as the fracture origins of the microcantilever beam specimens. It should be noted, however, that the above low Weibull modulus, 3.0–3.3, does not reflect that of bulk samples of Si_3N_4 ceramics, which is typically > 15 [66,67]. This is because in the bulk samples, totally different types of defects with much large sizes become the fracture origins, and the steeply rising *R*-curve behaviors due to grain-bridging effects are involved with strength determination and increase the Weibull modulus [68,69].

5. Conclusions

This study investigated the GB strengths for SN-Y, SN-La, and SN-Lu using the microcantilever beam specimens having the different angles, θ_{axis}, between the two intersecting-c-axes. As for SN-Y, the specimens (*S*) whose volume was ~1/6 of (*R*) were also used. The fractographic studies revealed that the fracture origins are divided into the target GBs and off-target ones. The former strengths, particularly those of SN-Y (*S*),

were so high that they were comparable to the theoretical values of the IGF strength estimated by computer simulations. The measured strength values were widely scattered for each of the samples, and the Weibull modulus was estimated to be 3.0 from the results of SN-Y (R) and (S). The GB strength depended on the type of RE and increased in order of Y<La<Lu, which was opposed to the predictions given by the CFS and DBE. It was suggested that the fracture occurs from the IGF/Si$_3$N$_4$ interfaces rather than within the IGF, and that O anions, which reside within the IGF and do not dissolve into the β-Si$_3$N$_4$ crystal lattice because of the high CFS, reduce the IGF/grain interface strength. This study also showed that the GB strength was little dependent on θ$_{axis}$ for all the three samples, contrary to the prediction that the high misorientation angle generates many dangling bonds at the IGF/Grain interfaces, lowering their strength. The suggested conceivable explanations were the formation of atomic short-range ordering at the interfaces, which likely helps accommodate the mismatch of the adjacent two grains, and the IGF accommodation ability, which resolves the mismatch with the relatively small thickness even at the high misorientation angles.

CRediT authorship contribution statement

Komaki Matsuura: Writing – original draft, Visualization, Investigation, Formal analysis, Data curation. **Tatsuki Ohji:** Writing – original draft, Visualization, Investigation. **Takuma Takahashi:** Writing – review & editing, Investigation. **Motoyuki Iijima:** Writing – review & editing, Investigation. **Junichi Tatami:** Writing – original draft, Validation, Supervision, Resources, Project administration, Methodology, Investigation, Funding acquisition, Conceptualization.

Declaration of Competing Interest

The authors declare that they have no known competing financial interests or personal relationships that could have appeared to influence the work reported in this paper.

Acknowledgements

References

[1] S. Hampshire, Silicon nitride ceramics, in: T. Ohji, M. Singh (Eds.), Engineered Ceramics, John Wiley & Sons, Inc., Hoboken, 2016, pp. 77–97, https://doi.org/10.1002/9781119100430.ch5.

[2] F.L. Riley, Silicon nitride and related materials, J. Am. Ceram. Soc. 83 (2000) 245–265, https://doi.org/10.1111/j.1151-2916.2000.tb01182.x.

[3] K. Komeya, Seeds innovation and bearing applications of silicon nitride ceramics, Ceram. Eng. Sci. Proc. 32 (2011) 1–15, https://doi.org/10.1002/9781118095379.ch1.

[4] H. Klemm, Silicon nitride for high-temperature applications, J. Am. Ceram. Soc. 93 (2010) 1501–1522, https://doi.org/10.1111/j.1551-2916.2010.03839.x.

[5] D.-W. Tan, L.-L. Zhu, W.-X. Wei, J.-J. Yu, Y.-Z. Zhou, W.-M. Guo, H.-T. Lin, Performance improvement of Si$_3$N$_4$ ceramic cutting tools by tailoring of phase composition and microstructure, Ceram. Inter. 46 (2020) 26182–26189, https://doi.org/10.1016/j.ceramint.2020.07.116.

[6] M.C. Anderson, R. Olsen, Bone ingrowth into porous silicon nitride, J. Biomed. Mater. Res. 92A (2010) 1598–1605, https://doi.org/10.1002/jbm.a.32498.

[7] J. Olofsson, T.M. Grehk, T. Berlind, C. Persson, S. Jacobson, H. Engqvist, Evaluation of silicon nitride as a wear resistant and resorbable alternative for total hip joint replacement, Biomatter 2 (2012) 94–102, https://doi.org/10.4161/biom.20710.

[8] D.T. Spencer, J.F. Bauters, J.E. Bowers, Integrated waveguide coupled Si$_3$N$_4$ resonators in the ultrahigh-Q regime, Optica 1 (2014) 153–157, https://doi.org/10.1364/OPTICA.1.000153.

[9] T. Yahagi, D. Kawai, T. Takahashi, M. Iijima, J. Tatami, Electrical resistivity of Si$_3$N$_4$ ceramics with Yb$_2$O$_3$ additive, J. Am. Ceram. Soc. 105 (2022) 2046–2057, https://doi.org/10.1111/jace.18211.

[10] Y. Nakashima, Y. Zhou, K. Tanabe, S. Arima, K. Hirao, T. Ohji, N. Murayama, M. Fukushima, Effect of microstructures on dielectric breakdown strength of sintered reaction-bonded silicon nitride ceramics, J. Am. Ceram. Soc. 106 (2023) 1139–1148, https://doi.org/10.1111/jace.18826.

[11] A.E. Kaloyeros, F.A. Jove, J. Goff, B. Arkles, Review - silicon nitride and silicon nitride-rich thin film technologies: trends in deposition techniques and related applications, ECS J. Solid State Sci. Technol. 6 (2017) 691–714, https://doi.org/10.1149/2.0011710jss.

[12] A.E. Kaloyeros, Y. Pan, J. Goff, B. Arkles, Review - Silicon Nitride and Silicon Nitride-Rich Thin Film Technologies: State-of-the-Art Processing Technologies, Properties, and Applications, ECS J. Solid State Sci. Technol. 9, 063006. https://doi.org/10.1149/2162-8777/aba447.

[13] A. Karttu, K. Lahtonen, J. Heikkilä, J. Väliaho, S. Narkilahti, J. Lekkala, P. Kallio, Corrosion and protection of silicon nitride insulators in microelectrode array applications, IEEE Sens. J. 22 (2022) 12504–12514, https://doi.org/10.1109/JSEN.2022.3178640.

[14] H. Kleebe, M.K. Chibulk, R.M. Cannon, M. Ruhle, Statistical analysis of the intergranular film thickness in silicon nitride ceramics, J. Am. Ceram. Soc. 76 (1993) 1969–1977, https://doi.org/10.1111/j.1151-2916.1993.tb08319.x.

[15] I. Tanaka, H.-J. Kleebe, M.K. Cinibulk, J. Bruley, D.R. Clarke, M. Rühle, Calcium concentration dependence of the intergranular film thickness in silicon nitride, J. Am. Ceram. Soc. 77 (1994) 911–914, https://doi.org/10.1111/j.1151-2916.1994.tb07246.x.

[16] H.-J. Kleebe, W. Braue, H. Schmidt, G. Pezzotti, G. Ziegler, Transmission electron microscopy of microstructures in ceramic materials, J. Eur. Ceram. Soc. 16 (1996) 339–351, https://doi.org/10.1016/0955-2219(95)00174-3.

[17] C.M. Wang, X. Pan, M.J. Hoffman, R.M. Cannon, M. Rühle, Grain Boundary films in rare-earth-glass-based silicon nitride, J. Am. Ceram. Soc. 79 (1996) 788–792, https://doi.org/10.1111/j.1151-2916.1996.tb07946.x.

[18] H.-J. Kleebe, Structure and chemistry of interfaces in Si$_3$N$_4$ ceramics studied by transmission electron microscopy, J. Ceram. Soc. Jpn. 105 (1997) 453–475, https://doi.org/10.2109/jcersj.105.453.

[19] E. Camposilvan, O. Torrents, M. Anglada, Small-scale mechanical behavior of zirconia, Acta Mater. 80 (2014) 239–249, https://doi.org/10.1016/j.actamat.2014.07.053.

[20] J. Tatami, M. Katayama, M. Ohnishi, T. Yahagi, T. Takahashi, T. Horiuchi, M. Yokouchi, K. Yasuda, D.K. Kim, T. Wakihara, K. Komeya, Local fracture toughness of Si$_3$N$_4$ ceramics measured using single-edge notched microcantilever beam specimens, J. Am. Ceram. Soc. 98 (2015) 965–971, https://doi.org/10.1111/jace.13391.

[21] A.D. Norton, S. Falco, N. Young, J. Severs, R.I. Todd, Microcantilever investigation of fracture toughness and subcritical crack growth on the scale of the microstructure in Al$_2$O$_3$, J. Eur. Ceram. Soc. 35 (2015) 4521–4533, https://doi.org/10.1016/j.jeurceramsoc.2015.08.023.

[22] S. Fujita, J. Tatami, T. Yahagi, T. Takahashi, M. Iijima, Degradation evaluation of Si$_3$N$_4$ ceramic surface layer in contact with molten Al using microcantilever beam specimens, J. Eur. Ceram. Soc. 37 (2017) 4351–4356, https://doi.org/10.1016/j.jeurceramsoc.2017.01.016.

[23] R. Henry, T. Blay, T. Douillard, A. Descamps-Mandine, I. Zacharie-Aubrun, J.-M. Gatt, C. Langlois, S. Meille, Local fracture toughness measurements in polycrystalline cubic zirconia using micro-cantilever bending tests, Mech. Mater. 136 (2019) 103086, https://doi.org/10.1016/j.mechmat.2019.103086.

[24] Y.-H. Ma, Z.-G. Wang, J.-H. Ouyang, S.J. Dillon, L. Feng, Y.-J. Wang, In-situ microcantilever deflection to evaluate the interfacial fracture properties of binary Al$_2$O$_3$/SmAlO$_3$ eutectic, J. Eur. Ceram. Soc. 39 (2019) 3277–3282, https://doi.org/10.1016/j.jeurceramsoc.2019.04.016.

[25] T. Csanádi, M. Vojtko, Z. Dankházi, M.J. Reece, J. Dusza, Small scale fracture and strength of high-entropy carbide grains during microcantilever bending experiments, J. Eur. Ceram. Soc. 40 (2020) 4774–4782, https://doi.org/10.1016/j.jeurceramsoc.2020.04.023.

[26] T. Csanádi, M. Gall, M. Vojtko, A. Kovalčíková, M. Hnatko, J. Dusza, P. Šajgalík, Microscale fracture strength of grains and grain boundaries in polycrystalline La-doped β-Si$_3$N$_4$ ceramics, J. Eur. Ceram. Soc. 40 (2020) 4783–4791, https://doi.org/10.1016/j.jeurceramsoc.2020.04.033.

[27] M. Tanabe, J. Tatami, M. Iijima, T. Yahagi, T. Takahashi, H. Nakano, T. Ohji, Deformation behaviors and fracture strength of β-Si$_3$N$_4$ single crystals, J. Am. Ceram. Soc. 106 (2023) 5431–5439, https://doi.org/10.1111/jace.19167.

[28] T. Csanádi, A. Azizpour, M. Vojtko, W.G. Fahrenholtz, The effect of crystal anisotropy on fracture toughness and strength of ZrB$_2$ microcantilevers, J. Am. Ceram. Soc. 107 (2024) 1669–1681, https://doi.org/10.1111/jace.19359.

[29] J. Tatami, M. Uda, T. Takahashi, T. Yahagi, M. Iijima, K. Matsui, T. Ohji, H. Nakano, Microscopic mechanical properties of silicon nitride ceramics corroded in sulfuric acid solution, J. Eur. Ceram. Soc. 44 (2024), https://doi.org/10.1016/j.jeurceramsoc.2023.11.072.

[30] T. Yahagi, T. Ohji, H. Yamaguchi, T. Takahashi, H. Nakano, M. Iijima, J. Tatami, Deformation behavior and fracture strength of single-crystal 4H-SiC determined by microcantilever bending tests, Adv. Eng. Mater. (2024) 2400095, https://doi.org/10.1002/adem.202400095.

[31] Y. Li, H.-N. Kim, H. Wu, M.-J. Kim, J.-W. Ko, Y.-J. Park, Z. Huang, H.-D. Kim, Microstructure and thermal conductivity of gas-pressure-sintered Si3N4 ceramic: the effects of Y$_2$O$_3$ additive content, J. Eur. Ceram. Soc. 41 (2021) 274–283, https://doi.org/10.1016/j.jeurceramsoc.2020.08.035.

[32] S. Li, H. Chen, W. Wang, D. Yao, Y. Xia, Y.-P. Zeng, Effects of Y$_2$O$_3$/MgO ratio on mechanical properties and thermal conductivity of silicon nitride ceramics, Int. J. Appl. Ceram. Technol. 19 (2022) 2873–2882, https://doi.org/10.1111/ijac.14067.

[33] R. Von Mises, Mechanik der plastischen Formaenderung von Kristallen, Z. Angew. Math. Mech. 8 (1928) 161–185, https://doi.org/10.1111/J.1151-2916.1991.TB07132.X.

[34] Y. Huang, J. Jiang, A critical review of von mises criterion for compatible deformation of polycrystalline materials, Crystals 13 (2023) 244, https://doi.org/10.3390/cryst13020244.

[35] S. Zhang, S.H. Garofalini, Effect of thickness of the intergranular film on fracture in Si3N4, J. Am. Ceram. Soc. 92 (2009) 147–151, https://doi.org/10.1111/j.1551-2916.2008.02815.x.

[36] S.H. Garofalini, S. Zhang, Molecular dynamics simulations of the effect of the composition of the intergranular film on fracture in Si3N4, J. Am. Ceram. Soc. 93 (2010) 235–240, https://doi.org/10.1111/j.1551-2916.2009.03400.x.

[37] W.Y. Ching, P. Rulis, L. Ouyang, S. Aryal, A. Misra, Theoretical study of the elasticity, mechanical behavior, electronic structure, interatomic bonding, and dielectric function of an intergranular glassy film model in prismatic β-Si3N4, Phys. Rev. B 81 (2010) 214120, https://doi.org/10.1103/PhysRevB.81.214120.

[38] P.F. Becher, G.S. Painter, E.Y. Sun, C.H. Hsueh, M.J. Lance, The importance of amorphous intergranular films in self-reinforced Si$_3$N$_4$ ceramics, Acta Mater. 48 (2000) 4493–4499, https://doi.org/10.1016/S1359-6454(00)00236-6.

[39] P.F. Becher, G.S. Painter, M.J. Lance, S. Ii, Y. Ikuhara, Direct observations of debonding of reinforcing grains in silicon nitride ceramics sintered with yttria plus alumina additives, J. Am. Ceram. Soc. 88 (2005) 1222–1226, https://doi.org/10.1111/j.1551-2916.2005.00237.x.

[40] G.S. Painter, P.F. Becher, W.A. Shelton, R.L. Satet, M.J. Hoffmann, Differential binding model: effects of rare-earths on β-Si3N4 grain growth and microstructure, 144108-1-4, Phys. Rev. B 70 (2004), https://doi.org/10.1103/PhysRevB.70.144108.

[41] G.B. Winkelman, C. Dwyer, T.S. Hudson, D. Nguyen-Mahn, M. Doblinger, R.L. Satet, M.J. Hoffmann, D.J.H. Cockayne, Arrangement of rare-earth elements at prismatic grain boundaries in silicon nitride, Philos. Mag. Lett. 84 (2004) 755–762, https://doi.org/10.1080/09500830500041302.

[42] G.B. Winkelman, C. Dwyer, T.S. Hudson, D. Nguyen-Mahn, M. Doblinger, R.L. Satet, M.J. Hoffmann, D.J.H. Cockayne, Three-dimensional organization of rare-earth atoms at grain boundaries in silicon nitride, Appl. Phys. Lett. 87 (2005), https://doi.org/10.1063/1.2009067, 061911-1–3.

[43] G.B. Winkelman, C. Dwyer, C. Marsh, T.S. Hudson, D. Nguyen-Mahn, M. Doblinger, D.J.H. Cockayne, The crystal/glass interface in doped Si3N4, Mater. Sci. Eng. A 422 (2006) 77–84, https://doi.org/10.1016/j.msea.2006.01.003.

[44] N. Shibata, G.S. Painter, R.L. Satet, M.J. Hoffmann, S.J Pennycook, P.F. Becher, Rare-earth adsorption at intergranular interfaces in silicon nitride ceramics: subnanometer observations and theory, Phys. Rev. B 72 (2005) 14101-1-4, https://doi.org/10.1103/PhysRevB.72.140101.

[45] K. van Benthem, G.S. Painter, F.W. Averill, S.J. Pennycook, P.F. Becher, Experimental Probe of Adsorbate Binding Energies at Internal Crystalline/Amorphous Interfaces in Gd-doped Si3N4, 16210-1–3, Appl. Phys. Lett. 92 (2008), https://doi.org/10.1063/1.2917566.

[46] R.L. Satet, M.J. Hoffmann, Influence of the rare-earth element on the mechanical properties of RE–Mg-bearing silicon nitride, J. Am. Ceram. Soc. 88 (2005) 2485–2490, https://doi.org/10.1111/j.1551-2916.2005.00421.x.

[47] R.L. Satet, M.J. Hoffmann, R.M. Cannon, Experimental evidence of the impact of rare-earth elements on particle growth and mechanical behavior of silicon nitride, Mater. Sci. Eng. A 422 (2006) 66–76, https://doi.org/10.1016/j.msea.2006.01.015.

[48] H. Gu, R.M. Cannon, I. Tanaka, M. Ruhle, Calcia partition in phase-separated intergranular glass and interfaces in doped silicon nitride produced by hot isostatic pressing, Mater. Sci. Eng. A 422 (2006) 51–65, https://doi.org/10.1016/j.msea.2006.01.012.

[49] P.F. Becher, G.S. Painter, N. Shibata, S.B. Waters, H.-T. Lin, Effects of Rare-Earth (RE) intergranular adsorption on the phase transformation, microstructure evolution, and mechanical properties in silicon nitride with RE$_2$O$_3$-MgO additives: RE=La, Gd, and Lu, J. Am. Ceram. Soc. 91 (2008) 2328–2336, https://doi.org/10.1111/j.1551-2916.2008.02448.x.

[50] Y. Zhou, H. Hyuga, D. Kusano, Y. Yoshizawa, T. Ohji, K. Hirao, Development of high-thermal-conductivity silicon nitride ceramics, J. Asian Ceram. Soc. 3 (2015) 221–229, https://doi.org/10.1016/j.jascer.2015.03.003.

[51] N. Hirosaki, S. Ogata, C. Kocer, H. Kitagawa, Y. Nakamura, Molecular dynamics calculation of the ideal thermal conductivity of single-crystal α- and β-Si3N4, Phys. Rev. B 65 (2002) 134110, https://doi.org/10.1103/PhysRevB.65.134110.

[52] M. Kitayama, K. Hirao, M. Toriyama, S. Kanzaki, Thermal conductivity of β-Si$_3$N$_4$: I, effects of various microstructural factors, J. Am. Ceram. Soc. 82 (1999) 3105–3112, https://doi.org/10.1111/j.1551-2916.1999.tb02209.x.

[53] M. Kitayama, K. Hirao, K. Watari, M. Toriyama, S. Kanzaki, Thermal conductivity of β- Si3N4: III, effect of rare-earth (RE = La, Nd, Gd, Y, Yb, and Sc) oxide additives, J. Am. Ceram. Soc. 84 (2001) 353–358, https://doi.org/10.1111/j.1551-2916.2001.tb00662.x.

[54] R.D. Shannon, C.T. Prewitt, Effective ionic radii in oxides and fluorides, Acta Cryst. B 25 (1969) 925–946, https://doi.org/10.1107/S0567740869003220.

[55] Y. Menke, V. Peltier-Baron, S. Hampshire, Effect of rare-earth cations on properties of sialon glasses, J. Non-Cryst. Solids 276 (2000) 145–150, https://doi.org/10.1016/S0022-3093(00)00268-4.

[56] D.M. Boye, C.P. Ortiz, A.J. Silversmith, N.T.T. Nguyen, K.R. Hoffman, Rare earth ion distribution in sol–gel silicate glasses, J. Lumines 128 (2008) 888–890, https://doi.org/10.1016/j.jlumin.2007.11.024.

[57] Y. Cheng, H. Xiao, W. Guo, Influence of rare-earth oxides on structure and crystallization properties of Bi$_2$O$_3$–B$_2$O$_3$ glass, Mater. Sci. Eng. A 480 (2008) 56–61, https://doi.org/10.1016/j.msea.2007.07.071.

[58] E.Y. Sun, P.F. Becher, K.P. Plucknett, C.H. Hsueh, K.B. Alexander, S.B. Waters, K. Hirao, M.E. Brito, Microstructural design of silicon nitride with improved fracture toughness: II, Effects of yttria and alumina additives, J. Am. Ceram. Soc. 81 (1998) 2831–2840, https://doi.org/10.1111/J.1151-2916.1998.TB02703.X.

[59] P.F. Becher, E.Y. Sun, C.-H. Hsueh, K.B. Alexander, S.-L. Hwang, S.B. Waters, C.G. Westmoreland, Debonding of interfaces between beta-silicon nitride whiskers and Si-Al-Y oxynitride glasses, Acta Mater. 44 (1996) 3881–3893, https://doi.org/10.1016/S1359-6454(96)00069-9.

[60] E.Y. Sun, P.F. Becher, C.-H. Hsueh, G.S. Painter, S.B. Waters, S.-L. Hwang, M.J. Hoffmann, Debonding behavior between β-Si3N4 whiskers and oxynitride glasses with or without an epitaxial β-SiAlON interfacial layer, Acta Mater. 47 (1999) 2777–2785, https://doi.org/10.1016/S1359-6454(99)00122-6.

[61] M. Yoshiya, K. Tatsumi, I. Tanaka, H. Adachi, Theoretical study on the chemistry of intergranular glassy film in Si3N4–SiO2 ceramics, J. Am. Ceram. Soc. 85 (2002) 109–112, https://doi.org/10.1111/j.1151-2916.2002.tb00049.x.

[62] W. Walkosz, R.F. Klie, S. Öğüt, B. Mikijelj, S.J. Pennycook, S.T. Pantelides, J.C. Idrobo, Crystal-induced effects at crystal/amorphous interfaces: the case of Si$_3$N$_4$/SiO$_2$, Phys. Rev. B 82 (2010) 081412, https://doi.org/10.1103/PhysRevB.82.081412.

[63] D.R. Lide. CRC Handbook of Chemistry and Physics, 89th ed., CRC Press, New York, 2009.

[64] D.R. Clarke, On the equilibrium thickness of intergranular glass phases in ceramic materials, J. Am. Ceram. Soc. 70 (1987) 15–22, https://doi.org/10.1111/j.1151-2916.1987.tb04846.x.

[65] M. Yoshiya, I. Tanaka, H. Adachi, R.M. Cannon, Theoretical study on the structure and energetics of intergranular glassy film in Si3N4-SiO2 ceramics, Int. J. Mater. Res. 101 (2010) 57–65, https://doi.org/10.3139/146.110240.

[66] J.A. Salem, S.R. Choi, M.R. Freedman, M.G. Jenkins, Mechanical behavior and failure phenomenon of an in situ toughened silicon nitride, J. Mater. Sci. 27 (1992) 4421–4428, https://doi.org/10.1007/BF00541575.

[67] N. Hirosaki, Y. Akimune, M. Mitomo, Effect of grain growth of β-silicon nitride on strength, weibull modulus, and fracture toughness, J. Am. Ceram. Soc. 76 (1993) 1892–1894, https://doi.org/10.1111/j.1151-2916.1993.tb06670.x.

[68] R.F. Cook, D.R. Clarke, Fracture stability, R-curves and strength variability, Acta Met. 36 (1988) 555–562, https://doi.org/10.1016/0001-6160(88)90088-0.

[69] D.K. Shetty, J.-S. Wang, Crack stability and strength distribution of ceramics that exhibit rising crack growth resistance (R-curve) behavior, J. Am. Ceram. Soc. 72 (1989) 1158–1162, https://doi.org/10.1111/j.1151-2916.1989.tb09700.x.